Title
Space-dependent temperature increase in human skin subsurface chromophores immediately following pulsed laser exposure

Authors
Nelson, JSMD
Milner, TE
Tanenbaum, BS
et al.

Publication Date
1996

SPACE DEPENDENT TEMPERATURE INCREASE IN HUMAN SKIN SUBSURFACE CHROMOPHORES IMMEDIATELY FOLLOWING PULSED LASER EXPOSURE

J. Stuart Nelson, Thomas E. Milner

Beckman Laser Institute and Medical Clinic
University of California, Irvine, CA 92715

B. Samuel Tanenbaum

Department of Engineering
Harvey Mudd College, Claremont, CA 91711

Dennis M. Goodman

Imaging Sciences Division
Lawrence Livermore National Laboratory, Livermore, CA 94550

ABSTRACT

Specifying the distribution of laser energy within a tissue is the first step toward understanding and capitalizing on a variety of laser-tissue interactions. Whether photothermal, photochemical, or photomechanical in nature, laser-tissue interactions begin with the absorption of photon energy. The spatial distribution of photon absorption specifies the required laser exposure to be delivered and the extent of subsequent therapeutic action. Using infrared tomography (IRT), the broad, long term objective of this research is the development of a three-dimensional tomographic reconstruction algorithm (TRA) as a means to determine the: (1) initial space-dependent temperature increase in subsurface chromophores ($\Delta T_{CHR}(\xi,\eta,\zeta,t=0)$) immediately following pulsed laser exposure; and (2) depths and physical dimensions of discrete subsurface chromophores. Analysis of the recorded time sequence of infrared emission images ($\Delta M_{CHR}(x,y,t)$) by longitudinal inversion and lateral deconvolution algorithms provides a direct means to determine the depths and physical dimensions of subsurface chromophores. Although our research is being shared with workers in a variety of disciplines, and pertinent to many clinical applications involving laser-induced photothermal mechanisms, we are particularly interested in addressing the problems associated with determination of the initial space-dependent temperature increase in subsurface chromophores in human skin in general, and port wine stain (PWS) blood vessels in particular.

2. BACKGROUND AND SIGNIFICANCE

2.1. Theory

Infrared tomography (IRT) uses a fast infrared focal plane array (IR-FPA) camera to detect temperature rises in a substrate, induced by pulsed radiation. The temperature rise, due to the selective optical absorption of pulsed laser light, creates an increase in infrared (blackbody) emission which is measured by a fast IR-FPA. Although IRT has become a topic of great interest in the physical sciences[1] for imaging subsurface cracks in aircraft fuselage due to metal fatigue, the application of this modality to determine the initial space-dependent temperature increase in individual subsurface chromophores in human skin immediately following pulsed laser exposure is novel[2]. For the purposes of IRT, chromophores in human skin can be modeled as a three-dimensional distribution of subsurface absorbing structures. In this model, when a pulsed laser source is used to irradiate the skin, an immediate increase in infrared emission will occur due to heating caused by optical absorption by the chromophores. An IRT record of human skin in response to pulsed laser exposure is composed of a time sequence of infrared emission images, that indicate localized heating of the subsurface chromophores (Figure 1). The absorbing chromophore's physical dimensions are best resolved in initial infrared emission images when lateral thermal diffusion is limited. Infrared emission in later images is more uniformly distributed in space due to lateral thermal diffusion.

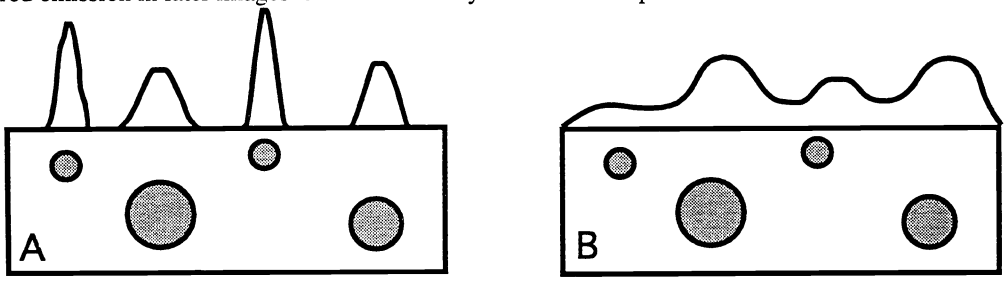

Figure 1: Infrared emission of model chromophores in human skin: (A) initial and (B) later image.

0-8194-1987-7/96/$6.00

The IRT integral equation (Eq. 1) can be written as a multi-dimensional convolution integral that relates the measured time sequence of infrared emission images ($\Delta M_{CHR}(x,y,t)$) to the initial space-dependent temperature increase ($\Delta T_{CHR}(\xi,\eta,\zeta,t=0)$) in subsurface chromophores immediately following pulsed laser exposure,

$$\Delta M_{CHR}(x,y,t) = \iint_{x',y'} K_c(x-x',y-y')dx'dy' \iiint_{\xi,\eta,\zeta} K_T(x'-\xi,y'-\eta,\zeta,t)\Delta T_{CHR}(\xi,\eta,\zeta,t=0)d\xi d\eta d\zeta$$
$$\Delta M_{CHR} = K_c * K_T * \Delta T_{CHR} \quad (1)$$

where $K_T(x-\xi,y-\eta,\zeta,t)$ and $K_C(x-\xi,y-\eta)$ represent, respectively, the thermal and camera point spread functions. Analysis of the recorded time sequence of infrared emission images ($\Delta M_{CHR}(x,y,t)$) by longitudinal inversion and lateral deconvolution algorithms provides a direct means to determine the depths and physical dimensions of subsurface chromophores.

2.2. Thermal and Camera Point Spread Functions

The important physical processes represented in the *IRT integral equation*, the thermal (K_T) and camera (K_C) point spread functions, are schematically illustrated in Figure 2.

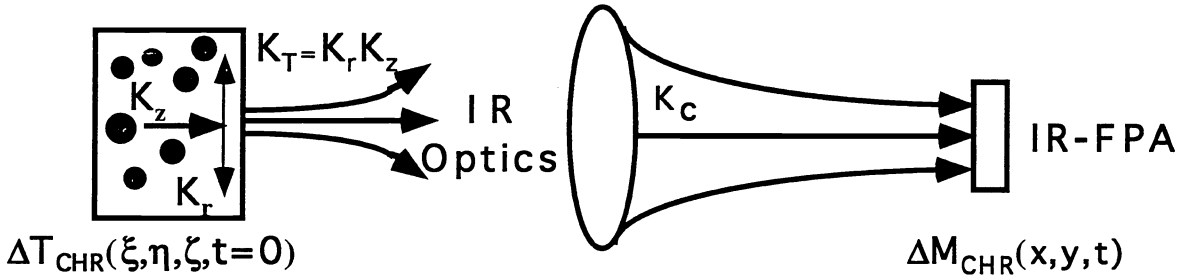

Figure 2: IRT record of model subsurface chromophores

Assuming a Dirac delta thermal source embedded in a biological material, solution of the bio-heat equation[3], gives the thermal point spread function K_T,

$$K_T(x-\xi,y-\eta,t,\zeta_o) = K_r(x-\xi,y-\eta,t)\cdot K_z(t,\zeta_o) \quad (2)$$

where the expression for K_T (Eq. 2) consists of two distinct terms (Eqs. 3a and 3b) that describe, respectively, heat diffusion along lateral (K_r) and longitudinal (K_z) axes.

$$K_r(x,y,t) = \frac{1}{2\pi(2\sigma_s^2 + 4\chi t)} e^{-(x^2+y^2)/(2\sigma_s^2+4\chi t)} \quad (3a)$$

$$K_z(t,\zeta_o) = \mu_{ir} e^{-\zeta_o^2/4\chi t}\left\{ erfcx(u_+) + erfcx(u_-) - \frac{2(h/\kappa)}{(h/\kappa)-\mu_{ir}}\cdot\left[erfcx(u_+) - erfcx(u_1)\right]\right\} \quad (3b)$$

Because the radiometric temperature at the tissue surface is not measured directly, we account for the inherent limitations of the IR-FPA camera and compute the camera point spread function (K_C) which includes effects due to size of the collection aperture, lens aberrations, finite number and size of discrete detector elements. Since the IR-FPA camera system uses a clear collection aperture and is an incoherent (i.e., thermal radiation) linear imaging system[4], the camera point spread function (K_C) is the Fourier transform (Eq. 4) of the modulation transfer function (MTF_C).

$$K_C = \Im(MTF_C);\quad MTF_C = MTF_D \cdot MTF_A \cdot MTF_0 \quad (4)$$

An analytic expression for MTF_C can be formed by a product of transfer functions representing the IR-FPA (MTF_D), lens aberrations (MTF_A), and camera optics (MTF_o).

2.3. Noise Equivalent Temperature Difference (NEΔT)

Successful development of an IRT instrument system for determining the initial space-dependent temperature increase in subsurface chromophores ($\Delta T_{CHR}(\xi,\eta,\zeta,t=0)$) immediately following pulsed laser exposure requires a realistic determination of the noise equivalent temperature difference (NEΔT). The accuracy to which our tomographic reconstruction algorithm (TRA) can determine the initial space-dependent temperature increase and depths and physical dimensions of subsurface chromophores depends directly on NEΔT.

In an optimized infrared detection system that measures radiometric temperature (i.e., 30-75°C), noise is limited by background emission fluctuations. The NEΔT (Eq. 5) is defined in terms of the numerical aperture $(NA)^2$ of the infrared imaging optics with geometric magnification factor m; detectivity ($D^*(\lambda)$) of the IR-FPA at infrared wavelengths λ; area (A_p) of each detector element; integration time (τ_i) of the camera readout electronics; emissivity [$\varepsilon(\lambda)$] of the object under test; and spectral radiant exitance ($M_\lambda(\lambda,T)$) of the source as given by Planck's law[5].

$$NE\Delta T = \frac{m}{(NA)^2\sqrt{\tau_i A_p}\int_{\lambda_1}^{\lambda_2} D^*(\lambda)\cdot\varepsilon(\lambda)\frac{\partial M_\lambda(\lambda,T)}{\partial T}d\lambda} \tag{5}$$

2.4. Application of IRT to Port Wine Stain (PWS)

The flashlamp-pumped pulsed dye laser (FLPPDL) has offered a superior approach in therapy due to its ability to destroy selectively port wine stain (PWS) blood vessels[6-8]. *However, only a small proportion of patients obtain 100% fading of their PWS, even after undergoing multiple laser treatments*[9-12]. The principal reason for poor results or treatment failure is that the pulse duration (0.45 ms) and light dosage ($\leq$ 10 J/cm^2) employed in current FLPPDL are, respectively, too short and too low to reach, and sustain over sufficient time, the critical core intravascular temperature necessary to destroy large PWS blood vessels irreversibly[13,14]. Improved therapeutic outcome in many patients is expected from the development of laser systems with longer pulse durations (0.25-15 ms) and higher light dosages ($\leq$ 25 J/cm^2). *Now that such laser systems have been developed, how will the clinician select the optimal pulse duration and light dosage of laser exposure for PWS therapy, on an individual patient basis, throughout an extended treatment protocol?*

Histopathological studies of PWS show a plexus of layers of dilated blood vessels located below the skin surface in the upper dermis. *PWS blood vessel diameters vary on an individual patient basis, and even from site to site on the same patient, over a range of 10-150 μm*[15]. The thermal relaxation time (τ_r) is defined as the time required for the core temperature, produced by the absorbed light energy within the target blood vessel, to cool to one-half of the original value immediately after the laser pulse and may be expressed

$$\tau_r = \frac{d_{BV}^2}{16\chi} \tag{6}$$

where d_{BV} is the diameter of the targeted blood vessel and χ is the thermal diffusivity of skin (1.1×10^{-7}m^2/s). For vessels with diameters of 10, 70 and 150 μm, τ_r has calculated values of 0.06, 2.8, and 12.8 ms, respectively. The pulse duration of laser exposure (t_p) governs the spatial confinement of heat and should, ideally, match the thermal relaxation time (τ_r) for the targeted blood vessels[16]. If longer pulse durations are employed ($t_p >> \tau_r$), heat diffuses outside the vessel during laser exposure. The target specificity is reduced resulting in nonspecific thermal damage to adjacent structures. Alternatively, if too short a laser pulse is used ($t_p << \tau_r$), high-peak intravascular temperature rises can produce explosive vaporization of tissue water, or photoacoustic transients which can result in vessel rupture. In such cases, repair mechanisms may revascularize the PWS. *In conclusion, selection of the correct pulse duration of laser exposure is crucial to successful blood vessel destruction. Only when $t_p \approx \tau_r$ can the critical core intravascular temperature, necessary to destroy large PWS blood vessels irreversibly, be achieved and sustained, for sufficient time.*

It is important to be aware that like pulse duration, *light dosage is also dependent on blood vessel diameter. For larger vessels, because energy deposition is limited by the optical penetration depth in whole blood $\left(\mu_a^{-1} = 30\ \mu m\right)$. Higher light dosages must be administered to reach, and sustain for sufficient time, the necessary critical core intravascular temperature*[14,17]. *Therefore, for the clinician to select the optimal light dosage as a function of pulse duration correctly, knowledge of the initial space-dependent temperature increase in subsurface PWS blood vessels ($\Delta T_{BV}(\xi,\eta,\zeta,t=0)$ immediately following pulsed laser exposure is required.*

For laser pulses in the millisecond domain, irreversible damage to PWS blood vessels occurs at core temperatures higher than 80^0C[14]. Once ΔT_{BV} has been determined from the IRT record in response to a *diagnostic sub-therapeutic laser pulse of duration t_0 and light dosage D_0*, the *therapeutic laser light dosage (D_{PWS})* necessary to destroy the PWS blood vessels can then be computed from equation 7 knowing the critical temperature increase, $\Delta T_C = 50^0C$ (assuming an ambient skin temperature of 30^0C).

$$D_{PWS} = D_o \frac{\Delta T_C}{\Delta T_{BV}} \frac{t_p}{t_o} \frac{\left(1 - e^{-t_0/\tau_r}\right)}{\left(1 - e^{-t_p/\tau_r}\right)} \tag{7}$$

For example, in response to a *diagnostic* laser pulse ($t_0 = 0.25$ ms and $D_0 = 5$ J/cm^2), the initial space-dependent temperature increase immediately following pulsed laser exposure (ΔT_{BV}) is determined from our three-dimensional tomographic reconstruction algorithm (TRA) to be 30^0C in PWS blood vessels with a mean diameter of 70 μm, inside the 5-7 mm circular beam spot of uniform light intensity. The *therapeutic* pulse duration *(t_p)* is calculated from equation 6 to be 2.8 ms. The *therapeutic* laser light dosage *(D_{PWS})* required to heat the 70 μm diameter PWS blood vessels to the critical core intravascular temperature (ΔT_C), necessary for destruction is then 12.6 J/cm^2 (Eq. 7).

The rationale for using IRT in the clinical management of patients with PWS is that the technique offers a means of documenting the vascular characteristics of PWS on a site to site basis for each patient. Prior to the institution of laser therapy, in response to a sub-therapeutic diagnostic laser pulse, analysis of the measured time sequence of emission images ($\Delta M_{BV}(x,y,t)$) contained within the IRT record at each PWS site by the TRA provides information on the: (1) initial space-dependent temperature increase ($\Delta T_{BV}(\xi,\eta,\zeta,t=0)$) within the blood vessels immediately following pulsed laser exposure; and (2) depths and physical dimensions of the most superficial absorbing PWS blood vessels inside the 5-7 mm circular beam spot of uniform light intensity. Such information can then be used by the clinician to help select the optimal parameters (pulse duration and light dosage) for the first laser treatment. Once the mean diameter of PWS blood vessels (d_{BV}) inside the 5-7 mm spot is determined from the deconvolved image, t_p can be calculated using equation 6. With $\Delta T_{BV}(\xi,\eta,\zeta,t=0)$ determined, the therapeutic laser light dosage (D_{PWS}) to destroy the PWS blood vessels can then be computed from equation 7. At the next patient visit, a second IRT record is made. Because the majority of the most superficial PWS blood vessels were obliterated by the first laser treatment, the diagnostic laser pulse now images a deeper absorbing layer of PWS blood vessels. The optimal parameters (pulse duration and light dosage) for the second laser exposure are selected based on analysis of the IRT record and a second treatment is performed. Proceeding in this manner, the IRT record probes deeper and deeper absorbing layers of the PWS after the most superficial layers are removed by each successive treatment at the same site.

3. PRELIMINARY RESULTS

3.1. IRT Integral Equation

The *IRT integral equation (Eq. 1)* forms the basis for our tomographic reconstruction algorithm (TRA) that estimates the initial space-dependent temperature increase in subsurface chromophores ($\Delta T_{CHR}(\xi,\eta,\zeta,t=0)$) immediately following pulsed laser exposure. As written, the *IRT integral equation* represents a *forward* problem in which the time sequence of measured infrared emission images ($\Delta M_{CHR}(x,y,t)$) may be computed from the initial space-dependent temperature increase ($\Delta T_{CHR}(\xi,\eta,\zeta,t=0)$) and the known biophysical properties of human skin. Our objective, however, is to determine the: (1) initial space-dependent temperature increase (i.e., $\Delta T_{CHR}(\xi,\eta,\zeta,t=0)$) immediately following pulsed laser exposure; and (2) depths and physical dimensions of subsurface chromophores. Inasmuch as only a time sequence of measured infrared emission images ($\Delta M_{CHR}(x,y,t)$) is available as input data, determination of $\Delta T_{CHR}(\xi,\eta,\zeta,t=0)$) in the IRT integral equation constitutes an *inverse* problem (Eq. 8).

$$\Delta T_{CHR} = (K_z)^{-1} \cdot (K_C * K_r)^{-1} \Delta M_{CHR} \tag{8}$$

3.2. Tomographic Reconstruction Algorithm (TRA)

A computationally efficient TRA is required to find a numerical solution [i.e., $\Delta T_{CHR}(\xi,\eta,\zeta,t=0)$] to the *IRT integral equation.* The size of the IRT problem restricts the selection of candidate algorithms; a typical IRT record of 100 infrared emission images, collected with a 128 x 128 IR-FPA camera, represents a vector containing N = 1.6 million components. We seek a method that incorporates the physical constraints of the problem to find a solution in a reasonable time period utilizing

affordable computing technology. We have developed computationally efficient *one-dimensional* longitudinal inversion and *two-dimensional* lateral deconvolution algorithms. Both algorithms are based on conjugate gradients and use a non-negativity constraint (i.e., $\Delta T_{CHR}(\xi,\eta,\zeta,t=0) \geq \mathbf{0}$) for improved solution estimates.

3.3. Longitudinal Inversion Problem

If the laser beam diameter is larger than both the thermal diffusion length and size of the infrared object field and a large number of closely spaced subsurface chromophores occupy the region of laser exposure, then heat propagation in the lateral direction can be averaged over a small central area (δA) and the IRT integral equation approximates a *one-dimensional* longitudinal integral equation (Eq. 9)

$$\Delta M_{CHR}^{1\text{-}D}(t) = \int_z K_z(t,z) \cdot \Delta T_{CHR}^{1\text{-}D}(z, t=0) dz \tag{9}$$

One-dimensional quantities $\Delta M_{CHR}^{1\text{-}D}(t)$ and $\Delta T_{CHR}^{1\text{-}D}(z, t=0)$ represent, respectively, the infrared emission image ($\Delta M_{CHR}(x,y,t)$) and the initial temperature increase ($\Delta T_{CHR}(\xi,\eta,\zeta,t=0)$) averaged over area δA positioned at the center of laser exposure (see computed simulation in Figure 3). The temperature change due to all subsurface chromophores at depth z (Eq. 10a), which is the solution to the longitudinal inverse problem $\left[Eq.\ 9;\ \Delta T_{CHR}^{1\text{-}D}(z, t=0)\right]$, is then equal to the area-weighted average of the temperature increase in discrete subsurface chromophores immediately following pulsed laser exposure (Eq. 10b)

$$\Delta T_{CHR}^{1\text{-}D}(z, t=0) = \iint_{\delta A} \sum_i \Delta T_i(\xi,\eta,z) d\xi d\eta / \delta A \tag{10a}$$

$$\Delta T_{CHR}^{1\text{-}D}(z, t=0) = \sum_i (\delta A_i / \delta A) \Delta T_i(z) \tag{10b}$$

where $\Delta T_i(z)$ and $\delta A_i/\delta A$ represent, respectively, the temperature increase and fractional area in the (ξ,η) plane at depth z of the i'th chromophore.

The *one-dimensional* longitudinal inversion equation (Eq. 9) can be approximated as a linear matrix problem in which the initial *one-dimensional* temperature increase $\left(\Delta T_{CHR}^{1\text{-}D}(z, t=0)\right)$ in subsurface chromophores and the longitudinal point spread function [K_z; Eq. 3b] are represented by, respectively, discrete *vector* and *matrix* quantities (Eq. 11); here, boldface symbols are used to represent vector and/or matrix terms.

$$\mathbf{\Delta M_{CHR}^{1\text{-}D} = K_z \cdot \Delta T_{CHR}^{1\text{-}D}} \tag{11}$$

The difficulty in computing a solution estimate for the initial *one-dimensional* temperature increase $\left(\Delta T_{CHR}^{1\text{-}D}(z, t=0)\right)$ in Eq. 11 stems from the large number of small singular values of the matrix $\mathbf{K_z}$[18]. Estimates for the unknown initial temperature increase can be obtained by minimizing $f(\Delta T_{CHR}^{1\text{-}D}, \Lambda)$ with respect to $\Delta T_{CHR}^{1\text{-}D}$ (Eq. 12). The regularization parameter (Λ) determines the degree of smoothening[19] and selection of its value is critical for determining optimum solution estimates.

$$f(\mathbf{\Delta T_{CHR}^{1\text{-}D}}, \Lambda) = \left\| \begin{bmatrix} \mathbf{K_z} \\ \sqrt{\Lambda} \end{bmatrix} \mathbf{\Delta T_{CHR}^{1\text{-}D}} - \begin{bmatrix} \mathbf{\Delta M_{CHR}^{1\text{-}D}} \\ 0 \end{bmatrix} \right\| \tag{12}$$

Because the initial temperature increase of discrete laser-heated subsurface chromophores is always positive $\left[\Delta T_{CHR}^{1\text{-}D}(z, t=0) \geq 0\right]$, we use a *non-negative constrained conjugate gradient algorithm* to compute solution estimates for the initial *one-dimensional* temperature increase, $\Delta T_{CHR}^{1\text{-}D}(\Lambda)$[20]. When using the algorithm, the quality of the solution estimate strongly depends on the regularization parameter (Λ). A number of techniques and philosophies exist for selecting Λ; briefly, we describe use of the L-curve approach[21]. Plotting the norm of the initial *one-dimensional* temperature increase, $\| \Delta T_{CHR}^{1\text{-}D}(\Lambda) \|$ against the residual norm, $\| \Delta M_{CHR}^{1\text{-}D} - \mathbf{K}\, \Delta T_{CHR}^{1\text{-}D}(\Lambda) \|$, was first suggested by Lawson and Hanson[22]. Typically as Λ increases from zero, $\| \Delta T_{CHR}^{1\text{-}D}(\Lambda) \|$ first rapidly decreases and $\| \Delta M_{CHR}^{1\text{-}D} - \mathbf{K}\, \Delta T_{CHR}^{1\text{-}D}(\Lambda) \|$ slightly increases. As Λ gets larger, then $\| \Delta T_{CHR}^{1\text{-}D}(\Lambda) \|$ slightly decreases and $\| \Delta M_{CHR}^{1\text{-}D} - \mathbf{K}\, \Delta T_{CHR}^{1\text{-}D}(\Lambda) \|$ rapidly increases. These two effects combine to yield an L-shaped

plot where the optimum regularization parameter (Λ) is at the corner of the L. We have developed a very fast method that estimates a solution to Eq. 12 by applying our algorithm to the unaugmented problem (Λ=0) and achieve regularization by *early termination* [20]. In this method, successive estimates of $\Delta T_{CHR}^{1-D}(\Lambda=0)$ are computed using a non-negative constrained conjugate gradient algorithm and the optimum iterate[23] is identified as the corner of the corresponding L-curve (i.e., plot of $\| \Delta T_{CHR}^{1-D}(\Lambda)\|$ vs. $\| \Delta M_{CHR}^{1-D} - \mathbf{K} \cdot \Delta T_{CHR}^{1-D}(\Lambda)\|$ for each iteration).

3.4. Lateral Deconvolution Problem

The *IRT integral equation* can be reduced to a *two-dimensional* inverse problem (Eq. 13a) in which the unknown [$\Delta T_{CHR}^{2-D}(t_0)$; Eq. 13b] represents the lateral space dependent temperature increase at time t_0 without blurring effects due to lateral thermal diffusion and the infrared optics.

$$\Delta M_{CHR}(x,y,t_0) = \iint_{\xi,\eta} K_L(x-\xi, y-\eta, t_0)\Delta T_{CHR}^{2-D}(\xi,\eta,t_0)d\xi d\eta \tag{13a}$$

$$\Delta T_{CHR}^{2-D}(\xi,\eta,t_0) = \int_z K_z(t_0,z)\cdot \Delta T_{CHR}(\xi,\eta,z,t=0)dz \tag{13b}$$

where the lateral point spread function (K_L) (Eq. 13c) accounts for blurring of subsurface chromophore images in human skin caused by lateral heat diffusion and limitations of the IR-FPA camera system.

$$K_L = K_C * K_R \tag{13c}$$

As in the case of the o*ne-dimensional* longitudinal inverse problem, a regularized matrix equation (Eq. 14) is written,

$$f(\Delta \mathbf{T}_{\mathbf{CHR}}^{\mathbf{2\text{-}D}}, \Lambda) = \left\| \begin{bmatrix} \mathbf{K_L} \\ \sqrt{\Lambda} \end{bmatrix} \Delta \mathbf{T}_{\mathbf{CHR}}^{\mathbf{2\text{-}D}} - \begin{bmatrix} \Delta \mathbf{M_{CHR}} \\ 0 \end{bmatrix} \right\| \tag{14}$$

Here $\Delta \mathbf{M_{CHR}}$ is a vector with N^2 components representing the infrared emission image recorded at time t_0 by individual detector elements in an N x N IR-FPA; $\mathbf{K_L}$ is an N^2 x N^2 matrix representing the lateral point spread function (K_L, Eq. 13c); and $\Delta \mathbf{T}_{\mathbf{CHR}}^{\mathbf{2\text{-}D}}$ is a N^2-component vector containing the unknown initial space dependent temperature increase in each discrete subsurface chromophore following pulsed laser exposure. The ill-posedness of the lateral inverse problem is due to attenuation of higher order spatial frequencies by inherent limitations of the IR-FPA camera system (Eq. 4; K_c) and lateral thermal diffusion (Eq. 3a; K_r). A variety of methods exist for solving linear least-squares imaging problems; however, the large dimension of the lateral inverse problem make our constrained conjugate gradient iterative method particularly attractive. We have developed an efficient spatial domain algorithm that implements successive iterations in the frequency domain, thus *significantly reducing the number of computations*[20]. The algorithm is based on conjugate gradients and uses a non-negativity constraint so as to eliminate "ringing" effects that often arise when using competing methods.

3.5. Layer-Stripping Method

Solutions to the longitudinal inverse problem [$\Delta T_{CHR}^{1-D}(z,t=0)$] can be applied to improve estimates of the lateral deconvolution problem when a *uniform* surface absorbing layer (e.g., epidermal melanin) overlies a distribution of deeper discrete chromophores (e.g., PWS blood vessels). In such cases, the temperature increase immediately following pulsed laser exposure in the surface absorbing layer [$\Delta T_S^{1-D}(z,t=0)$] is computed by solving the *one-dimensional* longitudinal inverse problem (Eq. 12) using our non-negative constrained conjugate gradient algorithm regularized by early termination. Knowledge of $\Delta T_S^{1-D}(z,t=0)$ allows computation (Eq. 15 of the infrared emission image [$\Delta M_S(x,y,t_0)$] exclusively due to the surface absorbing layer.

$$\Delta M_S(x,y,t_0) = \int_z K_z(t_0,z)\Delta T_S^{1-D}(z,t=0)dz \tag{15}$$

Infrared emission exclusively from the deeper discrete chromophores is then computed by subtracting $\Delta M_S(x,y,t_0)$ from a recorded infrared emission image $[\Delta M_{CHR}(x,y,t_0)]$. Solution of the lateral deconvolution problem [$\Delta T_{CHR}^{2\text{-}D}$,; Eq. 14] using the subtracted image $[\Delta M_{CHR}(x,y,t_0)-\Delta M_S(x,y,t_0)]$ as input data allows determination of the physical dimensions (δA_i) of discrete laser-heated subsurface chromophores. The mean temperature increase (ΔT_o) of discrete subsurface chromophores that consist of a single absorber (e.g., hemoglobin in blood) is computed (Eq. 16) from the fractional area [$f=\Sigma(\delta A_i/\delta A)$] and *one-dimensional temperature increase* [$\Delta T_{CHR}^{1\text{-}D}(z,t=0)$] as determined from, respectively, the solutions of the longitudinal inversion and lateral deconvolution problems.

$$\Delta T_o \approx \frac{\Delta T_{CHR}^{1\text{-}D}(z,t=0)}{f} \tag{16}$$

3.6. Model longitudinal inversion and lateral deconvolution algorithms

To test our longitudinal inversion and lateral deconvolution algorithms, we have formulated a general model system consisting of an arbitrary user-specified distribution of discrete subsurface chromophores in a composite multilayered structure. A model IRT problem has been formulated that allows numerical testing of our non-negative constrained conjugate gradient longitudinal inversion and lateral deconvolution algorithms. In our model, we assume that discrete subsurface chromophores of variable physical dimensions ($2a_i$,$2b_i$,$2c_i$=50-350 μm) are positioned beneath the skin surface (z_{CHR}=300±50 μm) and heated (ΔT_{CHR}= 40±5°C) in response to pulsed laser exposure. To simulate light absorption by epidermal melanin, we assume a uniform temperature increase (55°C) in an absorbing surface layer (z_s=10-75 μm). The temperature increase, depths, and physical dimensions of each chromophore are allowed to vary about mean values according to a uniform probability distribution. We have examined simulated infrared emission images ($\Delta M_{CHR}(x,y,t)$) collected by the camera system using f/1.5 infrared imaging optics with 2X magnification interfaced to a 128 x 128 IR-FPA with 50 x 50 mm² detector elements sensitive in the 3-5 μm spectral region.

From the time sequence of recorded infrared emission images ($\Delta M_{CHR}(x,y,t)$), we compute in Figure 3A the *one-dimensional* quantity $\Delta M_{CHR}^{1\text{-}D}(t)$ by averaging over an area (i.e., δA = 2 x 2 mm²) positioned at the center of laser exposure. Using our non-negative constrained conjugate gradient algorithm, we solve in Figure 3B the longitudinal inverse problem (Eq. 9) for the initial *one-dimensional* temperature increase $\Delta T_{CHR}^{1\text{-}D}(z,t=0)$. Temperature increases in the surface absorbing layer and deeper chromophores are clearly observed and differentiated in the computed *one-dimensional* solution $\Delta T_{CHR}^{1\text{-}D}$. Depths of the absorbing surface layer (z_S=50 μm) and deeper chromophores (z_{CHR}=300±50 μm) determined by our longitudinal inversion algorithm (Figure 3B) closely approximate the specified computer simulation depths.

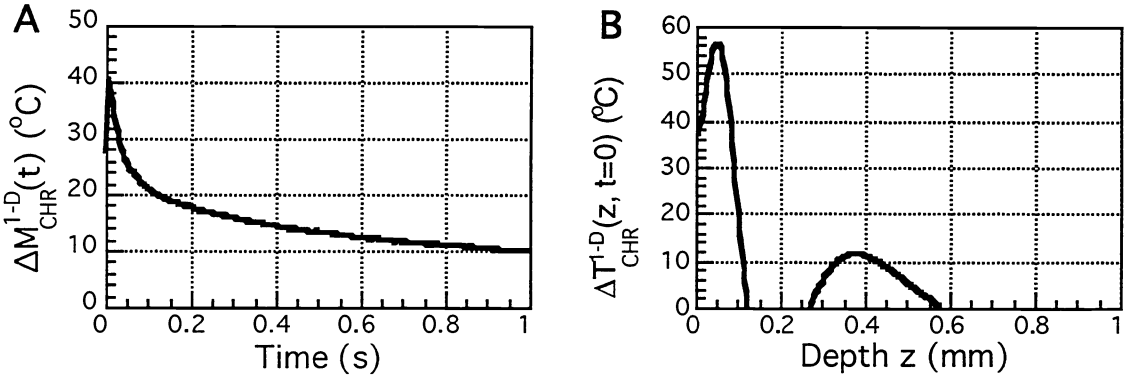

Figure 3: (A) Computed infrared emission, $\Delta M_{CHR}^{1\text{-}D}(t)$,; and (B) $\Delta T_{CHR}^{1\text{-}D}(z,t=0)$ as determined by our longitudinal inversion algorithm.

For the same distribution of chromophores used above in the *one-dimensional* longitudinal inverse problem, we compute (Eq. 13a) in Figure 4A $\Delta M_{CHR}(x,y,t_0 = 75\ ms)$. Infrared emission due to the surface absorbing layer [$\Delta M_S(x,y,t)$] is computed (Eq. 15) from the *one-dimensional* initial temperature increase $\Delta T_S^{1\text{-}D}(z,t=0)$ as determined by our longitudinal inversion algorithm. Infrared emission <u>*exclusively*</u> from the deeper discrete chromophores is computed by subtracting $\Delta M_S(x,y,t=75$

ms) from a recorded infrared emission image [$\Delta M_{CHR}(x,y,t=75\ ms)$] in Figure 4B. Solution of the lateral deconvolution problem (ΔT_{CHR}^{2-D}; Eq. 14) using the subtracted image [$\Delta M_{CHR}(x,y,t_0)$-$\Delta M_S(x,y,t_0)$] as input data allows determination of the physical dimensions (δA_i) of discrete laser-heated subsurface chromophores in Figure 4C. *Physical dimensions of discrete subsurface chromophores (d_{CHR}=50-350 μm) determined by our lateral deconvolution algorithm match the specified computer simulation dimensions (d=50-350 μm). The mean temperature increase (ΔT_o = 35°C) of laser-heated discrete subsurface chromophores was computed (Eq. 16) from the fractional area [f=0.32] and one-dimensional temperature increase [$\Delta T_{CHR}^{1-D}(z,t=0)$] as determined from, respectively, the solutions of the longitudinal inversion and lateral deconvolution problems.*

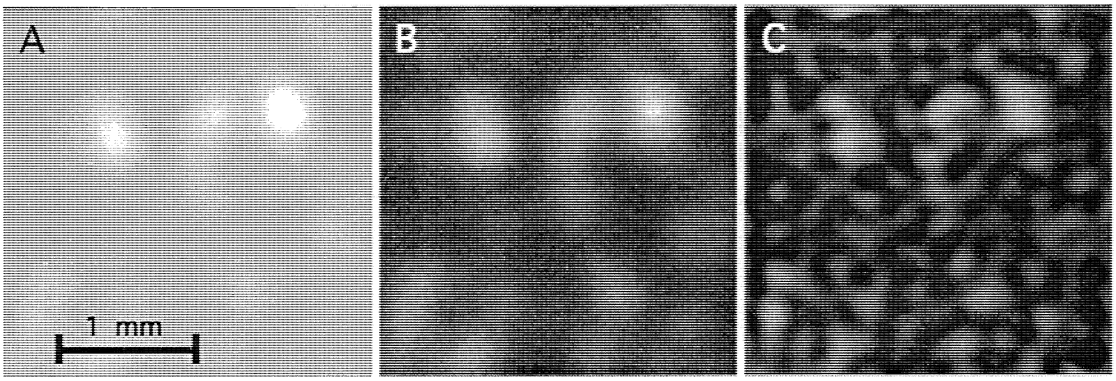

Figure 4: (A) Computed infrared emission, $\Delta M_{CHR}(x,y,t=75\ ms)$; (B) Infrared emission exclusively *from the deeper* discrete chromophores computed after application of layer-stripping method; (C) Solution of the lateral deconvolution problem ΔT_{CHR}^{2-D} using the subtracted image (B) as input data allows determination of the physical dimensions (δA_i) of discrete laser-heated subsurface chromophores.

4. EXPERIMENTAL RESULTS

Using in vitro and in vivo model chromophore systems, we have conducted a number of preliminary experiments that test the performance of our non-negative constrained conjugate gradient longitudinal inversion and lateral deconvolution algorithms. In each experiment, a 0.45 ms pulsed laser source (λ=585 nm) was used to expose a test material containing subsurface absorbing structures that simulate PWS blood vessels. A compound infrared lens (f/5, 50 mm diameter) imaged the surface increase in infrared emission intensity from the test material onto a 128 x 128 InSb IR-FPA. The camera system acquired 217 infrared emission images per second and was externally triggered by a digital delay generator that was optically triggered by a fast silicon photo receiver. The infrared signal collected by each detector element was digitized with a 3.5 MHz 12-bit (0-4,095) A/D converter and immediately stored in the computer's random access memory (Figure 5).

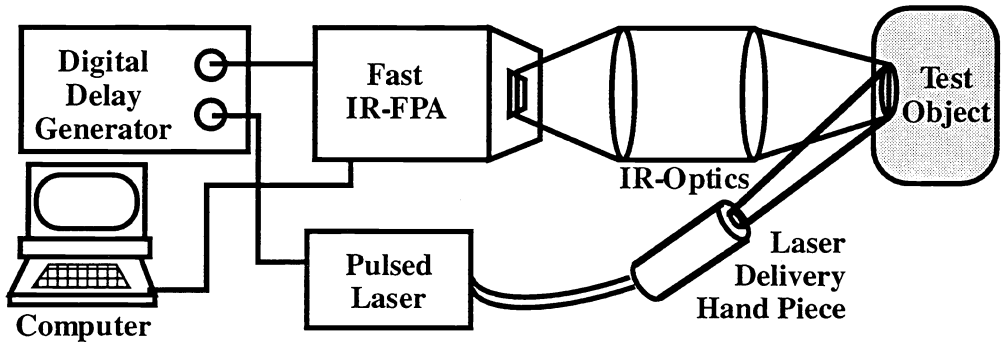

Figure 5: Schematic diagram of the IRT instrumentation for preliminary experiments.

4.1. In vitro PWS Model

A model phantom was constructed consisting of a number of closely spaced 175-225 μm diameter stained collagen strips (μ_a=20 mm^{-1}) positioned underneath two non-absorbing collagen films (total thickness; z_{CHR}=150±10 μm) and overlying a thick collagen sponge. Immediately following exposure to a 0.4 J laser pulse, a timed sequence of 100 infrared emission images ($\Delta M_{CHR}(x,y,t)$) was recorded over 460 ms. From this sequence, we determine in Figure 6A the *one-dimensional* quantity $\Delta M_{CHR}^{1\text{-}D}(t)$ by averaging over a circular area (δA =3.0 mm^2) positioned at the center of laser exposure. Using our non-negative constrained conjugate gradient algorithm (33 iterations), we solve in Figure 6B the longitudinal inverse problem (Eq. 9) for the initial *one-dimensional* temperature increase, $\Delta T_{CHR}^{1\text{-}D}(z,t=0)$, due to light absorption in the buried collagen strips. Depths of the collagen strips (z_{CHR}=150±20 μm) determined by our longitudinal inversion algorithm (Figure 6B) match the prepared model phantom (z_{CHR}=150±10 μm).

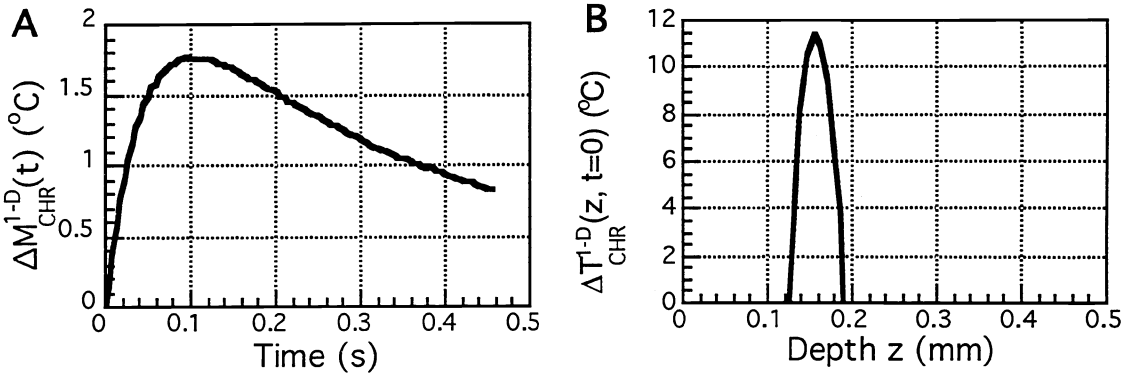

Figure 6: (A) Measured infrared emission, $\Delta M_{CHR}^{1\text{-}D}(t)$; (B) Depths of the buried collagen strips (z_{CHR}=150±20 μm) determined by our longitudinal inversion algorithm match those of the prepared model phantom (z_{CHR}=150±10 μm).

For the same phantom, infrared emission images $\left(\Delta M_{CHR}(x,y,t_o)\right)$ at 4.6 and 166 ms following pulsed laser exposure are shown in Figures 7A and 7B, respectively. Use of our non-negative constrained conjugate gradient algorithm (25 iterations) to solve the lateral deconvolution problem ($\Delta T_{CHR}^{2\text{-}D}$; Eq. 14) allows determination of the physical dimensions (δA_i) of discrete laser-heated buried collagen strips in Figure 7C by deconvolving the measured infrared emission image shown in Figure 7B to remove the effect of lateral blurring. *Physical dimensions of discrete collagen strips (d_{CHR}=175-225 μm) determined by our lateral deconvolution algorithm match the prepared model phantom dimensions (d_{CHR}=175-225 μm). The mean temperature increase (ΔT_o = 27.5 °C) in discrete laser-heated collagen strips was computed (Eq. 16) from the one-dimensional temperature increase [$\Delta T_{CHR}^{1\text{-}D}(z,t=0)$] and the fractional area [f=0.40] as determined from, respectively, the solutions of the longitudinal inversion and lateral deconvolution problems.*

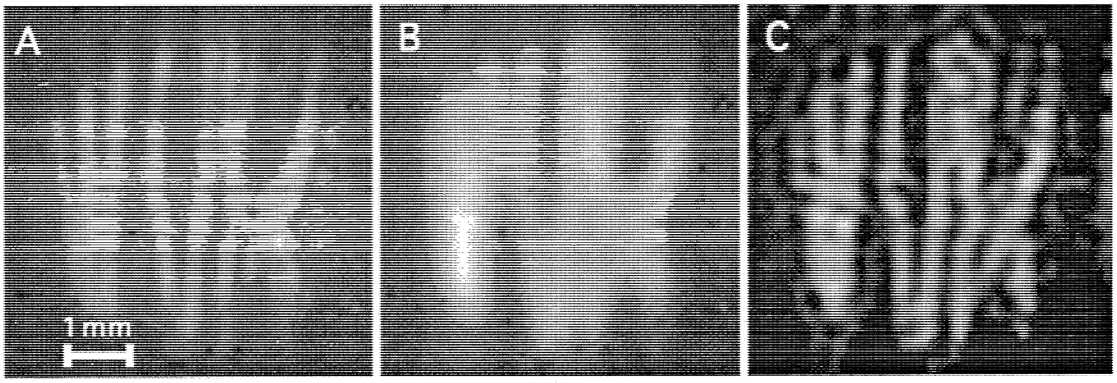

Figure 7: (A) Reference infrared emission image $\Delta M_{CHR}(x,y,t_0 = 4.6\ ms)$; (B) Measured infrared emission image $\Delta M_{CHR}(x,y,t_0 = 166\ ms)$; (C) physical dimensions of discrete collagen strips (d_{CHR}=175-225 μm) determined by our lateral deconvolution algorithm match the prepared model phantom dimensions.

4.2. In vivo Chick Chorioallantoic Membrane (CAM) Model

An aluminum mirror positioned directly above and oriented at 45° to the irradiated CAM surface imaged the infrared emission intensity from the microvasculature into the IR-FPA camera system. Immediately following exposure to a 1.0 J laser pulse, a timed sequence of 140 infrared emission images ($\Delta M_{BV}(x,y,t)$) was recorded over 660 ms. From this sequence, we determine in Figure 8A the *one-dimensional* quantity $\Delta M_{BV}^{1\text{-}D}(t)$ by averaging over an area (δA =1.5 mm^2) positioned at the center of laser exposure. Using our non-negative constrained conjugate gradient algorithm (20 iterations), we solve in Figure 8B the longitudinal inverse problem (Eq. 9) for the initial *one-dimensional* temperature increases, $\Delta T_{BV}^{1\text{-}D}(z,t=0)$, in the surface absorbing layer of capillaries ($z_{BV} \leq 25$ μm) and deep lying venules ($z_{BV} = 300 \pm 75$ μm).

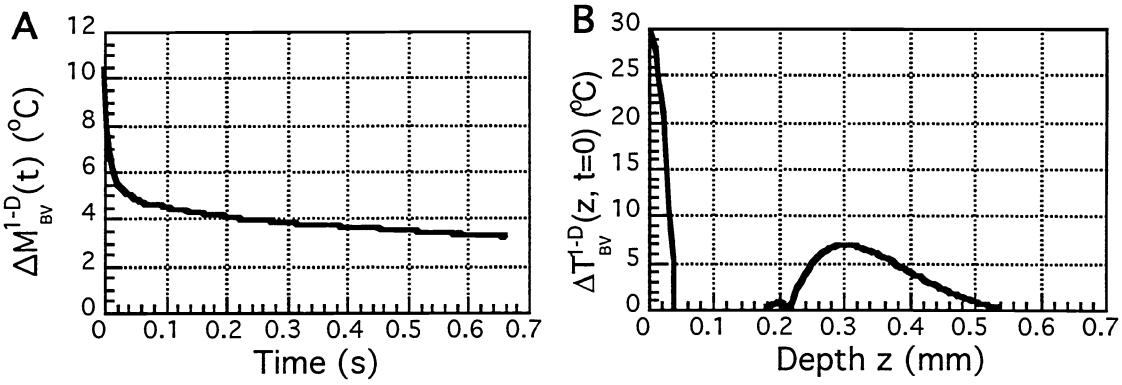

Figure 8: (A) Measured infrared emission, $\Delta M_{BV}^{1\text{-}D}(t)$; (B) Depths of surface capillaries ($z_{BV} \leq 25$ μm) and deep lying venules ($z_{BV} = 300 \pm 75$ μm) as determined by our longitudinal inversion algorithm.

For the same plexus of deep venules, we measured in Figure 9A $\Delta M_{BV}(x,y,t_0 = 32\ ms)$. Infrared emission *exclusively* from the plexus of deep (z_{BV}= 300 μm) lying venules is computed by subtracting $\Delta M_S(x,y,t_0=32$ ms) from a recorded infrared emission image [$\Delta M_{BV}(x,y,t_0=32$ ms)] in Figure 9B. Solution of the lateral deconvolution problem ($\Delta T_{CHR}^{2\text{-}D}$; Eq. 14) using the subtracted image [$\Delta M_{BV}(x,y,t_0) - \Delta M_S(x,y,t_0)$] as input data allows determination of the physical dimensions (δA_i) of discrete laser-heated deep venules in Figure 9C. *Physical dimensions of discrete deep venules (d_{BV}=150-200 μm) determined by our lateral deconvolution algorithm match the dimensions measured directly using light microscopy. The mean temperature increase (ΔT_o = 33°C) of laser-heated discrete venules was computed (Eq. 16) from the fractional area [f=0.32] and one-dimensional temperature increase [$\Delta T_{BV}^{1\text{-}D}(z,t=0)$] as determined from, respectively, the solutions of the longitudinal inversion and lateral deconvolution problems.*

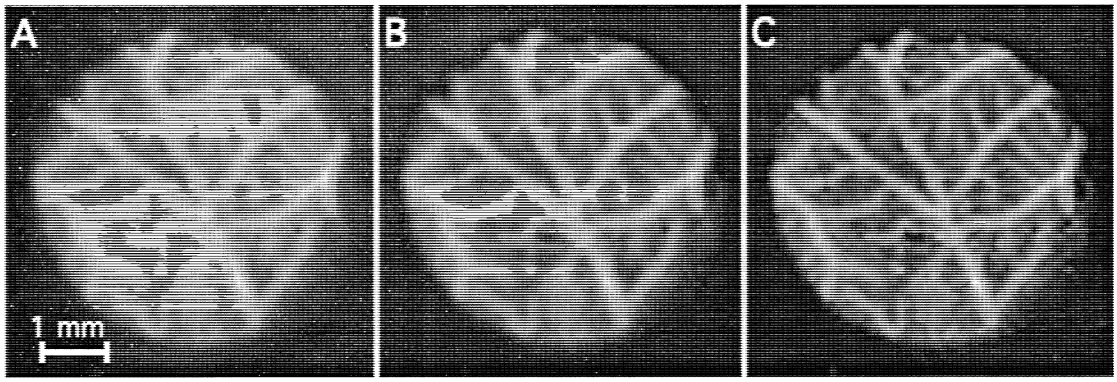

Figure 9: (A) Measured infrared emission image $\Delta M_{BV}(x,y,t_0 = 32\ ms)$; (B) Infrared emission *exclusively* from the deep (z_{BV}=300 μm) venules computed after application of layer-stripping method; (C) Solution of the lateral deconvolution problem $\Delta T_{BV}^{2\text{-}D}$ using the subtracted image (B) as input data allows determination of the physical dimensions (δA_i) of deep venules; dimensions (d_{BV}=150-200 μm) determined by our lateral deconvolution algorithm match the dimensions measured directly using light microscopy.

4.3. PWS Patient IRT Measurements

We have verified the use of the high-speed IR-FPA camera system to image individual laser-heated PWS blood vessels. Immediately following exposure to a 1.0 J laser pulse (5.0 J/cm^2), the IR-FPA camera system recorded a timed sequence of 126 infrared emission images ($\Delta M_{bv}(x,y,t)$). From this sequence, we determine in Figure 10A the *one-dimensional* quantity $\Delta M_{BV}^{1\text{-}D}(t)$ by averaging over an area (δA = 1.5 mm^2) positioned at the center of laser exposure. Using our non-negative constrained conjugate gradient algorithm, we solve in Figure 10B the longitudinal inverse problem (Eq. 9) for the initial *one-dimensional* temperature increases, $\Delta T_{BV}^{1\text{-}D}(z,t=0)$, in the epidermal melanin layer and deeper PWS blood vessels. Depths of the epidermal melanin layer (z_S=50±25 μm) and deeper PWS blood vessels (z_{BV}=275±75 μm) determined by our longitudinal inversion algorithm (Figure 10B) match the mean depths measured directly using histopathology.

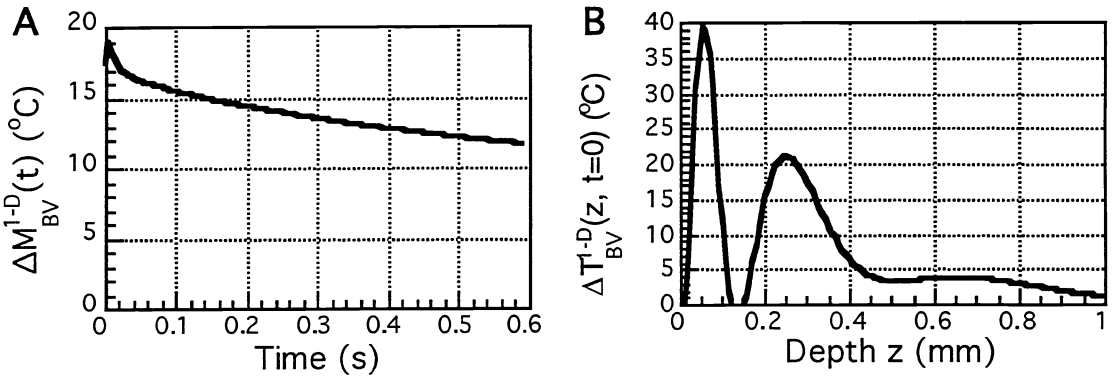

Figure 10: (A) Measured infrared emission, $\Delta M_{BV}^{1\text{-}D}(t)$; (B) Depths of the epidermal melanin layer (z_s=50±25 μm) and PWS blood vessels (z_{BV}=275±75 μm) determined by our longitudinal inversion algorithm match the mean depths measured directly using histopathology.

For the same PWS site, we measured in Figure 11A $\Delta M_{BV}(x,y,t_0 = 77\ ms)$. Infrared emission *exclusively* from the deep PWS blood vessels is computed by subtracting $\Delta M_S(x,y,t_0$=77 ms) from a recorded infrared emission image [$\Delta M_{BV}(x,y,t_0$=77 ms)] in Figure 11B. Solution of the lateral deconvolution problem ($\Delta T_{CHR}^{2\text{-}D}$; Eq. 14) using the subtracted image [$\Delta M_{BV}(x,y,t_0)$-$\Delta M_S(x,y,t_0)$] as input data allows determination of the physical dimensions (δA_i) of discrete laser-heated deep PWS blood vessels in Figure 11C. *Physical dimensions of discrete PWS blood vessels were determined by our lateral deconvolution algorithm to be 150-200 μm. The mean temperature increase (ΔT_0 = 48°C) of laser-heated discrete PWS blood vessels was computed (Eq. 16) from the fractional area [f=0.42] and one-dimensional temperature increase [$\Delta T_{BV}^{1\text{-}D}(z,t=0)$] as determined from, respectively, the solutions of the longitudinal inversion and lateral deconvolution problems.*

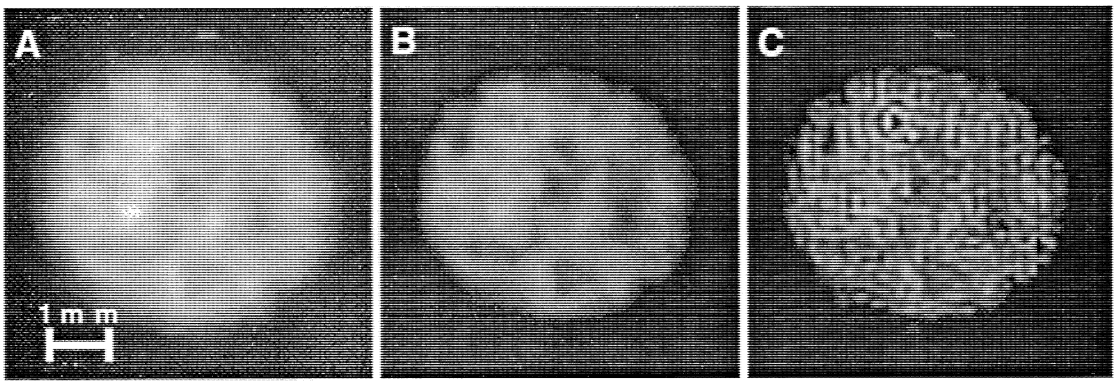

Figure 11: (A) Measured infrared emission image $\Delta M_{BV}(x,y,t_0 = 77\ ms)$; (B) Infrared emission exclusively *from the deeper* discrete PWS blood vessels computed after application of layer-stripping method; (C) Solution of the lateral deconvolution problem $\Delta T_{BV}^{2\text{-}D}$ using the subtracted image (B) as input data; physical dimensions (δA_i) of discrete PWS blood vessel were determined by our lateral deconvolution algorithm to be 150-200 μm.

5. ACKNOWLEDGMENTS

This project was supported by research grants awarded from the Biomedical Research Technology Program (R03-RR06988) and Institute of Arthritis and Musculoskeletal and Skin Diseases (1R29-AR41638-01A1 and 1R01-AR42437-01A1) at the National Institutes of Health, Whitaker Foundation, and Dermatology Foundation to JSN. Institutional support from the Office of Naval Research, Department of Energy, National Institutes of Health, and the Beckman Laser Institute and Medical Clinic Endowment is also gratefully acknowledged. The authors would also like to thank Lars O. Svaasand, Ph.D., Sol Kimel, Ph.D., and Steven L. Jacques, Ph.D. for many helpful discussions.

6. REFERENCES

1. Favro, LD, Ahmed, T, Wang, L, Wang, X, Kuo, PK, Thomas, RL, Shepard, SM. Thermal wave imaging of aircraft structures. In: Review of Progress in Quantitative NDE, Thompson, DO, Chimenti, D, (eds.). 1994, in press.
2. Milner, TE, Norvang, LT, Svaasand, LO, Tran, N, Tanenbaum, BS, Nelson, JS. Photothermal tomography of subcutaneous chromophores. SPIE 1993;2077: 228-236.
3. Carslaw, HS, Jaeger, JC. Conduction of heat in solids. New York, NY: Oxford University Press, 1959.
4. Goodman, JW. Introduction to Fourier Optics, San Francisco: McGraw Hill, 1968.
5. Hopper, GS. Forward looking infrared systems, In: Infrared and Electro-Optical Handbook, Vol. 5, Campana, SB (ed.), Ann Arbor, MI: Infrared Information and Analysis Center, 1993:103-155.
6. Ashinoff, R, and Geronemus, RG. Flashlamp-pumped pulsed dye laser for port wine stains in infancy: earlier versus later treatment. J. Am. Acad. Dermatol. 1991; 24: 467-472.
7. Nelson, JS, and Applebaum, J. Clinical management of port-wine stain in infants and young children using the flashlamp-pulsed dye laser. Clin. Pediatrics 1990; 29: 503-508.
8. Nelson, JS. Selective photothermolysis and removal of cutaneous vasculopathies by pulsed laser. Plast. Reconstr. Surg. 1991; 88: 723-731.
9. Garden, JM, Polla, LL, Tan, OT. The treatment of port wine stains by the pulsed dye laser. Arch. Dermatol. 1988; 124: 889-896.
10. Reyes, BA, and Geronemus, RG. Treatment of port-wine stains during childhood with the flashlamp-pumped dye laser. J. Am. Acad. Dermatol. 1990; 23: 1142-1148.
11. Ashinoff, R, and Geronemus, RG. Capillary hemangiomas and treatment with the flashlamp-pulsed dye laser. Arch. Dermatol. 1991; 127: 202-205.
12. Geronemus, RG. Pulsed dye laser treatment of vascular lesions in children. J. Dermatol. Surg. Oncol. 1993; 19: 303-310.
13. Nelson, JS, Milner, TE, Anvari, B, Tanenbaum, BS, Kimel, S, Svaasand, LO. Dynamic epidermal cooling during pulsed laser treatment of port wine stain - a new methodology with preliminary clinical evaluation. Arch. Dermatol. 1995;131:695-700.
14. van Gemert, MJC, Welch, AJ, Miller, ID, Tan, OT. Can physical modeling lead to an optimal laser treatment strategy for port-wine stains? In: Laser Applications in Medicine and Biology, Wolbarsht, M (ed.). New York, NY: Plenum Press, 1991:199-275.
15. Barsky, SH, Rosen, S, Geer, DE, Noe, JM. The nature and evolution of port wine stains: a computer assisted study. J. Invest. Dermatol. 1980;74:154-157.
16. Anderson, RR, and Parrish, JA. Selective photothermolysis: precise microsurgery by selective absorption of pulsed radiation. Science 1983; 220:524-527.
17. Kimel, S, Svaasand, LO, Hammer-Wilson, M., Schell MJ, Milner, TE, Nelson, JS, Berns, MW. Differential vascular response to laser photothermolysis. J. Invest. Dermatol. 1994;103:693-700.
18. Milner, TE, Goodman, DM, Tanenbaum, BS, Nelson, JS. Depth profiling of laser heated chromophores in biological tissues using pulsed photothermal radiometry. J. Optical Soc. America A 1995;12:1479-1488.
19. Groetsch, CW. The theory of regularization for Frefholm equations of the first kind, Marshfield, MA: Pitman Press, 1984.
20. Goodman, DM, Johansson E, Lawrence TW. On applying the conjugate-gradient algorithm image processing problems. In: Multivariate Analysis: Future Directions, Rao, CR (ed.). Amsterdam: North-Holland Press, 1992.
21. Hansen, PC, and O'Leary, DP. The use of the L-curve in the regularization of discrete ill-posed problems. J. Sci. Comput. 1993;14:1487-1503.
22. Lawson, CL, and Hanson, RJ., Solving Least Squares Problems., Englewood Cliffs, NJ: Prentice Hall, 1974.
23. Frank, IE, and Friedman, JH. A statistical view of some chemometrics regression tools. Technometrics 1993;35:109-148.